THE HFCTR DEMONSTRATION REACTOR DESIGN STUDY: ADVANTAGES OF HIGH FORCE DENSITY MAGNETS AND TOTAL MODULARIZATION

J. H. Schultz, F. S. Malick, D. R. Cohn,
and J. E. C. Williams

November 1979

PFC/RR-80-3

This paper was presented at the "8th Symposium on Engineering Problems of Fusion Research", San Francisco, Calif., Nov. 13 - 16, 1979.

THE HFCTR DEMONSTRATION REACTOR DESIGN STUDY: ADVANTAGES OF HIGH FORCE DENSITY MAGNETS AND TOTAL MODULARIZATION

J.H. Schultz and F.S. Malick
Westinghouse Electric Corporation
Pittsburgh, PA 15236

D.R. Cohn and J.E.C. Williams
Massachusetts Institute of Technology
Cambridge, MA 02139

Summary

A conceptual design has been developed for a moderate size (R_o = 6.0 m) high field (B_t = 13.1 T at the coil) tokamak demonstration power reactor which can produce fusion power densities as high as 10 MW/m^3 with a spatially averaged value of toroidal beta of less than 5%. The High Field Compact Tokamak Reactor (HFCTR) design is based upon minimal extrapolation from experimentally established plasma confinement and MHD stability in tokamak devices. The product of average current density and maximum field in the toroidal field coils is shown to be a fundamental figure of merit for tokamaks. A unique design of the Nb_3Sn toroidal-field magnet system allows the achievement of high fields with a small radial build. An integrated system of automated actuators, vacuum and current-carrying mechanical joints and flexible cryostats allow total modularization of the reactor, including the poloidal and toroidal field coil systems. A detailed estimate of maintenance operation time indicated the possibility of performing all mechanical operations in a 45° sector replacement in two days. The modest value of toroidal beta permits a simple plasma-shaping coil system, with only two coil pairs inside the TF coil bore. The plasma is initiated by rapidly dropping a pre-existing bias field in the interior coils. Heating of the central plasma is attained by the use of vertically asymmetric coils for ripple-assisted injection of 120 keV D^o beams, which are also used for dynamic control of the plasma temperature during the burn period. A FLIBE-lithium blanket is designed for high power-density operation in a high field environment and gives an overall tritium breeding ratio of 1.05.

Introduction

The objective of the High Field Compact Tokamak Reactor (HFCTR) design study was to examine potential advantages and problems associated with the use of high performance, high field (≈13 T at the coil) superconducting magnets in a commercial tokamak reactor. High performance magnets allow the formation of high fusion power density plasmas in relatively compact devices at modest levels of beta [1,2].

Tokamak Engineering Figures of Merit

Engineering figures of merit have been developed as a means of guiding and assessing the HFCTR design, a figure of merit is defined as a parameter of a system which causes the desirability of the system to increase as the figure increases over a broad range of possible designs. Figures of merit are useful in the study of commercial tokamak reactors, because the systems are so complex, the design space so broad and the design goal so far in the future that numerical costing methods provide limited guidance. Two engineering figures of merit associated with reactor design have previously achieved general acceptance -- wall loading on the plasma first wall (P_w) and plant availability (p.a.). In addition, we propose that the product of the average current density in the inner leg of the toroidal field magnet and the maximum field at the toroidal field coil, $\bar{J}\ B_{MAX}$, is an important figure of merit.

While probably not as important as the former figures of merit, $\bar{J}\ B_{MAX}$, combines with P_w and P_w x(p.a) to form a complete set. The set is complete in that simultaneous increases in these three figures can be shown to cause simultaneous, monotonic decreases in the three economic

cost figures: cost, cost/kWe and cost/kWh. The fundamental goodness of $\bar{J} \times B_{MAX}$ has been argued[3], using the simplifying case of reactors with relatively small OH bores. For this case, it was shown that many key measures of plasma performance, such as the $n\tau_e$, predicted by empirical scaling, $n\tau_e \sim n^2 a^2$[1], fusion power density, gross electric power, wall loading and alpha containment increased only as rapid functions of $\bar{J} B_{MAX}$, reactor size and some optimizable function of reactor geometry. For example, if C is the ratio of the radius of maximum field at the coils to the plasma major radius and ε is the inverse aspect ratio, then the wall loading P_w, with β_t proportional to ε, scales as:

$$P_w \sim \beta^2 B_t^4 a \sim B_T^4 \varepsilon^2 a \sim (JB)^2 C^6 \varepsilon^3 R_o^3$$

where B_t is the flux density at the plasma magnetic axis and a is the plasma minor radius. Since $C^6 \varepsilon^3$ is zero when either C or ε equals one, this quantity has a maximum value for any value of R_o, the plasma major radius. Therefore, for a given size device, the wall-loading can be further increased only by increasing $\bar{J} B_{MAX}$. Conversely, the major radius can be decreased for a given value of P_w, only by increasing $\bar{J} B_{MAX}$.

Major Features of the HFCTR Design

The major features of the HFCTR design are consistent with the above-mentioned figures of merit. The final conceptual design significantly increased $\bar{J} B_{MAX}$ over that of other reactor designs, as shown in Table I, equalled the wall-loading and increased the projected plant availability over that in the previous generation of reactor designs.

J x B was increased by the following methods:

(1) Use of Nb_3Sn superconductor.

(2) Use of vertical reactions through the reactor central column to reduce tensile stress in the inside legs of the TF coils.

(3) Use of additional plate material in the "knee of the D" along with external horizontal reactions to reduce bending-induced stresses.

(4) Use of new experimental information on transient recovery to reduce the helium pumping power associated with a given level of heat transfer in a system cooled by the forced-flow of supercritical helium.

(5) Use of lattice-braided superconducting cable to even the flow of helium coolant to each conductor strand.

(6) Use of well-characterized design techniques and experimental information developed through Westinghouse participation in the Large Coil Program.

High first-wall thermal loading has been achieved by the following methods:

(1) Use of a high heat capacity, low pumping power coolant, such as a lithium salt.

(2) Use of a high maximum temperature, refractory structural material.

(3) Use of a thick copper coating on the first-wall coolant tubes to reduce thermal stresses.

(4) Use of bracketed thin tubes, unconstrained along their axes to reduce bending stresses, as the first wall facing the plasma.

(5) Use of a double vacuum vessel; the structural wall holding the first wall coolant tubes separates the medium vacuum blanket region from the high vacuum plasma region.

High plant availability, compatible with high wall-loading and a need for frequent replacement of a module is achieved by the following methods:

(1) Total modularization; every subsystem included in a 45° modular sector can be rapidly and automatically removed and replaced, not just the blanket and first wall.

(2) Simultaneous, automated replacement of all modules reduces the down-time associated with routine first wall and blanket replacements.

(3) Replacement of manipulator-based maintenance by automatic actuator-based maintenance techniques.

(4) Use of flexible cryostats; TF dewars can collapse and form a monolithic toroidal structure with the central cylinder and each other on energization of the TF coils.

(5) Use of flat multilam copper joints, allowing zero-insertion formation of inside joints in poloidal field coils.

(6) Use of double vacuum wall and mechanical vacuum seals.

Additional Design Features

The HFCTR design includes several novel features, other than those highlighted above.

(1) Asymmetric Ripple Injection. In order to remove the requirement for high beam voltage, a controlled toroidal-field ripple is used to enhance the penetration of energetic ions formed by near-vertical injection of 120 keV D^{o} beams.

(2) Pulsed Nulling-Field Coils. The principal equilibrium-field coils are superconducting, unpulsed and operated continuously, while a separate copper nulling coil system provides the necessary field during start-up. The nulling coil system reduces the pulsed power stored energy requirement as only the vertical field in the volume immediately surrounding the plasma is pulsed. This system leads to a unique circuit topology. Taking into account topological differences, mutual coupling and a complete plasma scenario, a trade study indicated that the poloidal field power conditioning system would be about 45% more expensive without the use of a null coil.[3]

(3) Simple, modularized plasma shaping-coil system. The plasma equilibrium is achieved with only three coil pairs, during steady-state burn. A superconducting hexapole field plasma shaping coil is located in the ohmic heating coil core, thereby eliminating the need for placement of relatively inaccessible copper coils on the inside of the vacuum chanber. The copper coils located inside the bore of the TF moduler are segmented with electrical connections formed by pressure contacts.

Reactor Parameters

The reference HFCTR parameters are shown in Table II. Because of the use of high field (7.4 T) at the plasma magnetic axis, the plasma achieves high specific power density (7.7 MW/m^3) and neutron wall-loading (3.4 MW/m^2) with only a modest total beta (β0.04%). The reactor reference parameters reflect a normal operating condition of a highly flexible reactor, which can produce thermal power levels as high as 3,300 MW or as low as 1000 MW, and achieve ignition with a toroidal beta as low as 2.5%. The reactor is relatively small, with a major radius of 6.0 m and a minor radius of 1.2 m.

The time-averaged thermal power output of the reactor is 2470 MW. Assuming 35% thermal-to-electric conversion efficiency, the gross electric power is 870 MW. The net electric power is only 612 MW, largely because of high, parasitic losses in the poloidal field system. A 500 second burn and consequent high duty cycle is specified, although a magnetic divertor is not used. The high ignition margin of the reactor permits significant build-up of helium and wall impurities before extinction is required. An oblique limiter before the vacuum pumping port is used to allow the vacuum system to achieve the alpha removal effectiveness of $\sim$ 20% necessary for the 500 second burn.

The Toroidal Field System

Key features of the toroidal field magnet system are shown in figures 1, 2 and 3. The HFCTR magnet system parameters are listed in Table III. The maximum flux density at the toroidal field coil is 13.1 T. At this flux density, the critical properties of Nb_3Sn are beginning to degrade rapidly. However, by proper disposition of materials, a total force density can be achieved which is greater than that of previous designs.

The basic "rope in a pipe" conductor used in the Westinghouse LCP coil was used in the HFCTR design. The high surface area of this concept and its intrinsic scaleability to higher current, without decreasing the surface to volume ratio, makes it particularly well-suited to a high-field, high-energy application in the presence of a.c. pulsed fields. The ability to place ground-wall insulation around each conductor allows higher discharge voltages on quench, minimizing the stabilizer protection requirement beyond that required for recovery on quench. The distributed structure of bolted plates with machined slots allows the conductor to have the substantial strength in bending, required for "constant-tension" TF coils of significant thickness. The distributed structure also permits the coil to be placed closer to the plasma than does a winding on a bobbin. The cooling system, consisting of forced-flow, supercritical helium, uses as many parallel hydraulic channels as possible, in order to maximize the system's steady-state heat-removal capability.

The TF system uses a flexible cryostat, as shown in figure 3. Flexibility in two planes is provided by a simple bellows, consisting of

a single loop of spring steel, as shown in figure 4. The bellows are compressed by charging the TF coils and are forced open by screw-jack actuators, permanently installed on the TF coil transporters. If necessary, electric heating elements in the joints and the steel cryostat walls are heated electrically to remove frozen air, before disengaging a coil module. Compression of the flexible cryostats removes dead space from the radial build between the toroidal field coils and the cryogenically-cooled bucking cylinder and the ohmic heating coil system. It also permits a press fit to be made to thick top and bottom end caps, which permit tensile load sharing with a vertically continuous, laminated central steel core. Centering and bending-induced stresses are reduced to a lesser extent by the reaction through the end flanges of forces on diametrically opposite D-coils.

Automated Disassembly

As indicated in the previous section, the entire mechanical design of the HFCTR reactor is determined by the goal of rapid, automatic mechanical assembly and disassembly. All mechanical operations are performed by permanently installed actuators, with no need for motion to the assembly/disassembly area, setting up of lights and cameras or identification of the parts to be removed or installed. No welds must be made or cut between modules. Press fits between large, flexible surfaces eliminate the need for critical alignments of bolts and boltholes. TF coil modules are precooled to 4.2 K with the flexible cryostats extended, weeks before scheduled assembly, so that cooldown time does not contribute to reactor down-time.

The overall mechanical support structure of a module is shown in Figure 5 in elevation view. Each two coil module is supported by a transporter with retractable rollers, allowing radial and circumferential motion of the module. Tensile forces in the TF coil inner leg are shared through the structural core end cap by a flexible cryostat on the structural core, which can be compressed to allow removal of the module. The shield, blanket and interior EF coils are supported by a bore component support frame, resting on a platform support. The neutral beam injector is supported from a basement transporter and can be retracted below the reactor cell floor, which is then bridged, prior to module movement. The ohmic heating coils, bucking cylinder and central structural core share a common, flexible cryostat, which becomes a common cold-space with the TF modules on energization of the coils. The bucking cylinder consists of wedged bricks, in order to minimize eddy currents. The ohmic heating coils are stacked pancakes, with electrical and coolant leads on the outside of the ohmic heating coil. The structural core consists of flat, laminated steel plates, welded and off-set near the reactor equator to provide the top-bottom continuity needed for load-sharing.

Automated reassembly of finger-joints in the inside equilibrium field coils is probably the most critical alignment during reactor reassembly. The joint concept is shown in figure 6. Flat multilam contacts were tested early in the TFTR program and were shown to have a lifetime of 500,000 pulses for a 1 cm deflection[3] and are incorporated here to minimize the needed contact pressure and to reduce alignment tolerances. Flexible sheet copper sections flank the multilam joints,

in order to permit misalignment as great as $\pm$ 1.0 cm, before assembly. Clamps and pressure pads mounted on the bore component support frame create a rigid conductor, after assembly.

Sniderman's parallel studies of module replacements with manipulators[4] and with actuators[3] decomposed each operation down to the level of the torquing of a single bolt and concluded that the mechanical operations of a module replacement would require several months with manipulators and two days with in-place actuators. Detritiation of the vacuum vessel walls prior to opening vacuum seals and re-establishment of high vacuum after reassembly were not included in the analysis. While the fundamental limitations on the speed with which detritiation and pumpdown could be accomplished has not been determined, a related study indicates that an additional one to two weeks of down-time may be necessary for each module replacement.[5]

The effect of the unavoidable down-time associated with each module replacement on reactor availability can be minimized by replacing all modules simultaneously. Replacement of a single module would occur only in the case of unscheduled faults. Figure 7 depicts a possible queuing of the modules, during simultaneous replacement, which avoids unnecessary down-time due to "traffic jams." The letters O and N represent old and new modules respectively, while the numbers represent assembled positions in the clockwise direction. In comparison with replacement of a single module, simultaneous replacement of all modules has the following advantages:

(1) Scheduled downtime is reduced by almost a factor of the number of modules.

(2) Residual radioactivity in the reactor cell is greatly reduced, easing the possibility of making critical alignments, when necessary, by hands-on or shielded-cab maintenance.

(3) The lifetime of the first generation of modules is increased by a factor of $2N^2/N\ (N+1)$, where N is the number of modules; similarly the spare modules need not be purchased and assembled until the actual end-of-life of all modules.

Summary

The HFCTR reactor study examined many novel concepts, deserving of further study. However, two conclusions in particular best summarize the results of the study:

(1) Increasing the force density of the TF coils can have a first-order beneficial effect on reactor economics, irrespective of the value of coil field or plasma beta.

(2) It is not impossible to conceive of a tokamak reactor design with negligible downtime due to scheduled maintenance.

References

1. D.R. Cohn, R.R. Parker and D.L. Jassby, Nuclear Fusion 16, 31 (1976).
2. D.R. Cohn, D.L. Jassby, R.R. Parker and J.E.C. Williams, "A High Density High Field Tokamak Demonstration Power Reactor", Proc. of ANS Topical Conf. on Technology of Controlled Fusion, Richland, Washington, 1976.
3. D.R. Cohn, J.H. Schultz, et al., "High Field Compact Tokamak Reactor (HFCTR) Conceptual Design", M.I.T. Plasma Fusion Center Report RR-79-2; January 1979.
4. M. Sniderman, "Fusion Reactor Remote Maintenance Study", EPRI-ER-1046; April, 1979.
5. R.J. Temkin, et al., "Design Study of an ECRH System for a Tokamak Power Reactor", M.I.T. Plasma Fusion Center Report PFC/RR-79-20, 1979.

$\bar{J} \times B_{MAX}$ of previous reactor designs (as shown in Figure 1-1), equals the wall-loading and increases the plant availability over that in the previous generation of reactor designs.

J x B has been increased by the following methods:

(1) Use of Nb_3Sn superconductor. We have also examined the consequences of using a more advanced superconductor, such as $Nb_3(Sn_{1-x}\ Ga_x)$.

(2) Use of vertical reactions through the reactor central column to reduce tensile stress in the inside legs of the TF coils.

(3) Use of additional plate material in the "knee of the D" along with external horizontal reactions to reduce bending-induced stresses.

(4) Use of new experimental information to derive a new and encouraging correlation for the Nusselt number for multi-stranded cable in supercritical helium.

(5) Use of lattice-braided superconducting cable for even flow of helium coolant to each conductor strand.

(6) Use of well-characterized design techniques and experimental information developed through Westinghouse participation in the Large Coil Program.

First-wall thermal loading (MW/m^2) has been increased by the following methods:

(1) Use of a high heat capacity, low pumping power coolant, such as FLIBE.

(2) Use of a high maximum temperature structural material, such as TZM.

TOKAMAK	B_{MAX}	$\bar{J}$	$\bar{J}B_{MAX}$
UWMAK I	8.7 T	8.05 MA m^{-2}	69.7
UWMAK II	8.3 T	7.39 MA m^{-2}	61.3
UWMAK III	8.75 T	8.77 MA m^{-2}	76.7
GA EPR	8.0 T	12.7 MA m^{-2}	101
NUWMAK	11.9 T	11.7 MA m^{-2}	138
HFCTR	13.1 T	12.2 MA m^{-2}	160

Table I Force Densities in Conceptual Superconducting Toroidal Field Coil Designs for Tokamak Power Reactors.

TABLE II

REFERENCE HFCTR PARAMETERS

Machine Parameters	
Major radius, R_o (m)	6.0
Plasma halfwidth, a(m)	1.2
Aspect ratio	5.0
Plasma shape factor, S	1.5
Field at plasma, B_T(T)	7.4
Maximum field at winding, B_{T_o}(T)	13.1
Plasma volume, V_p(m^3)	317
First wall area, A_W(m^2)	475
Plasma Parameters	
Safety factor at r = a, q(a)	3.0
Average toroidal beta, $\langle\beta_T\rangle$	0.04
Plasma current, (MA)	6.7
Electron density, n(m^{-3})	$5.2 \times 10^{20}(1 - \frac{r^3}{a^3})$
Electron ion temp, T (keV)	$12.4\ (1 - \frac{r^2}{a^2})$
Z_{eff} (Helium + Mo)	1.2
$(\bar{n}\tau_E)_{emp}/(\bar{n}\tau_E)_{ign}$	2.4
Beam Power, P_b(MW)	100
Beam Energy, W_b(keV)	120
Power Production	
Av. fusion power density, $\bar{P}_f$(MW/m^3)	7.7
14-Mev neutron wall loading, P_W(85% duty, MW/m^2)	3.4
Total fusion power, $\bar{P}_f V_p$	2440
Av. thermal power, P_{th} (85% duty, MW)	2470

TABLE 1 - I

REFERENCE HFCTR PARAMETERS (CONT.)

Machine Parameters

Gross electric power, P_g (35% efficiency, MW)	870
Net electric power, P_n (MW)	775
Plant efficiency, η_p (%)	31

TABLE III

HFCTR TOROIDAL FIELD COIL MAJOR PARAMETERS

Number of Coils	16
Current in Each Coil	13.9 MA
Peak Field on Winding	13.1 T
Coil Vertical Bore	10.5 m
Coil Horizontal Bore	6.5 m
Number of Turns	1200
Current per Conductor	11.75 kA
Conductor Width (outside of insulation & jacket)	2.088 cm
Conductor Height (outside of insulation & jacket)	2.088 cm
Conductor Jacket Thickness	0.089 cm
Conductor Insulation Thickness	0.055 cm
Coil Build (inner leg)	1.0 m
Coil Build (outer leg)	1.27 m
Number of Pancakes	27
Pancake Structural Material	310 S
Number of Splits per Pancake	9
Number of Slots per Full Plate	6
Plate Thickness	5.179 cm
Number of Bolts Between Overlapping Splits	8
Number of Bolts Across Plate Width	
inner leg	6
outer leg	10
Bolt Diameter	2.54 cm
Bolt Material	A-286
	40% Cold Worked

3.2 TOROIDAL FIELD COIL DESIGN

3.2.1 Basic Design Features

The proposed toroidal field coil shape and design ensure that each component performs a necessary function under the combined operating conditions of toroidal field and poloidal field loading. The basic coil shape is that of a D-shaped winding path within the specified dimensions, as shown in Figure 3-3. The inner straight leg of the coil has a trapezoidal cross section, consisting of segmented plates with grooves for locating the conductor, bolted together to form an integral structure. The outer leg of the coil has a retangular cross section of plate segments bolted together. This rectangular cross section, however, has a trapezoidal winding cross section as shown in Figure 3-3 for ease in manufacturing and winding of the coil.

The D-shaped winding was chosen to obtain the advantage of constant tension over the entire coil circumference. Another major advantage of the D-shape is that the straight leg is available to support the high centering force which dominates the forces in toroidal field coils and for ease in manufacture and assembly.

The selected coil design is a pancake configuration consisting of overlapping segmented plates as shown in Figure 3-4. Overlapping of the pancake segments is arranged so that the splits at any particular location occur in only every third pancake as shown in Figure 3-4. This arrangement reduces the amount of load which must be transfered through the bolts without exceeding the available plate sizes. Overlapping of the plates enables the entire coil to be held together by bolts passing through the plates.

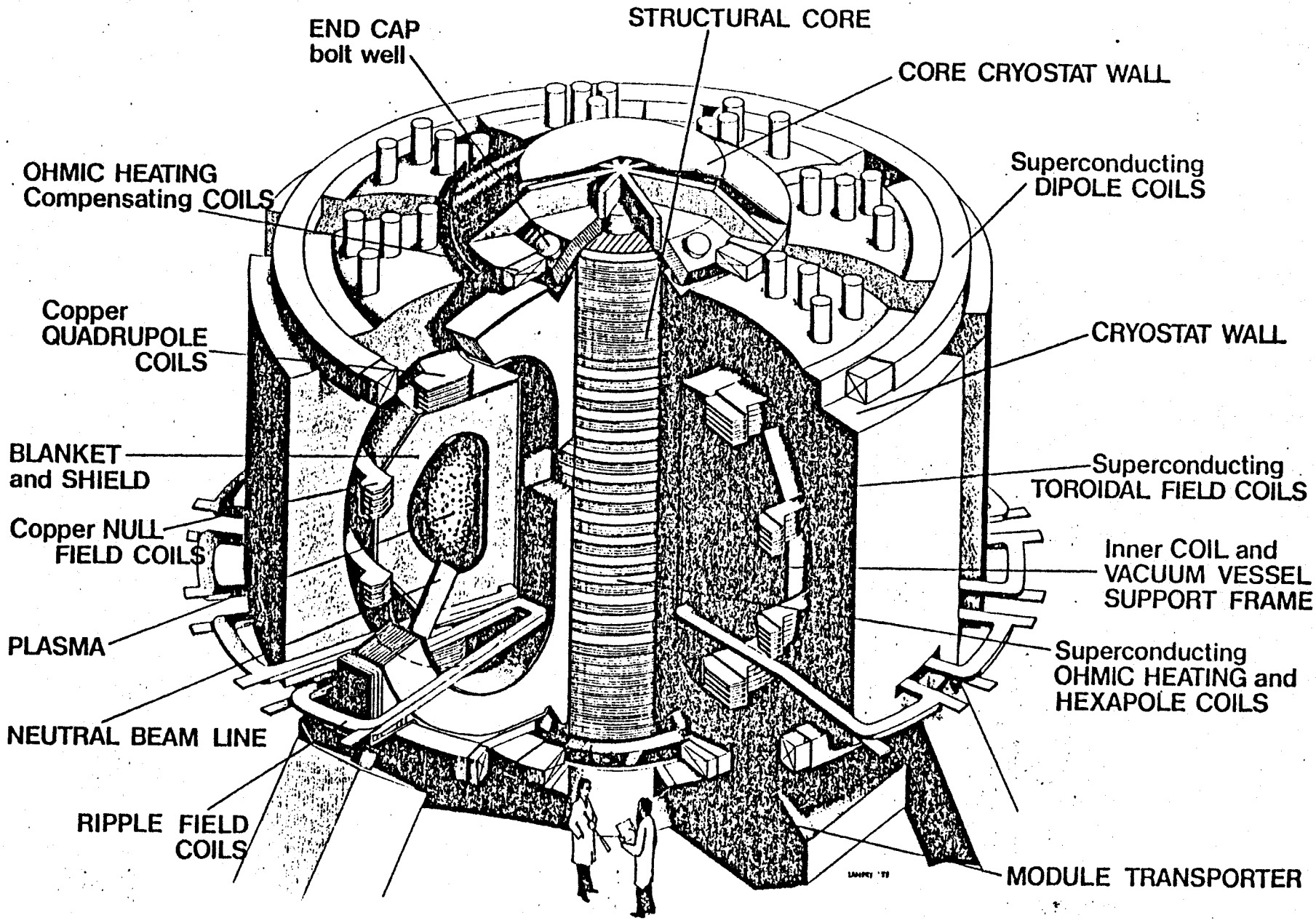

Figure 1 The High Field Compact Tokamak Reactor (HFCTR)

3. MAGNET SYSTEM

3.1 DESIGN FEATURES

The basic magnet system design is guided by the need to deal with the large forces created by the high field operation and the requirement that the magnet system be modularized in order to facilitate disassembly and maintenance. Additional constraints are that the pulse power requirements, the power dissipation resulting from copper coil operation, and the refrigeration losses in the superconducting magnet portion be kept within reasonable bounds.

The magnet system design which has been developed to meet these guidelines is shown in Figure 3-1. It differs from conventional designs in a number of ways:

(1) Forces between diametrically opposed toroidal field (TF) D coils are supported at the top and bottom of the trunk by means of circular end caps. As a result, the tensile force transmitted to the center straight sections of the toroidal field coils is greatly reduced. This makes possible a compact design while keeping the maximum strain in the superconductor to less than 0.1%. This is a conservative value, since experiments [1,2] show that strains of 0.2% are possible. The toroidal field coil conductor is shown in Figure 3.2 [3].

(2) The primary equilibrium field (EF) coils, i.e. the dipole coils, are DC, superconducting, and continuously operating. During start-up and shut-down, the changing EF is provided by driving a copper coil system to oppose the DC dipole coils. In addition,

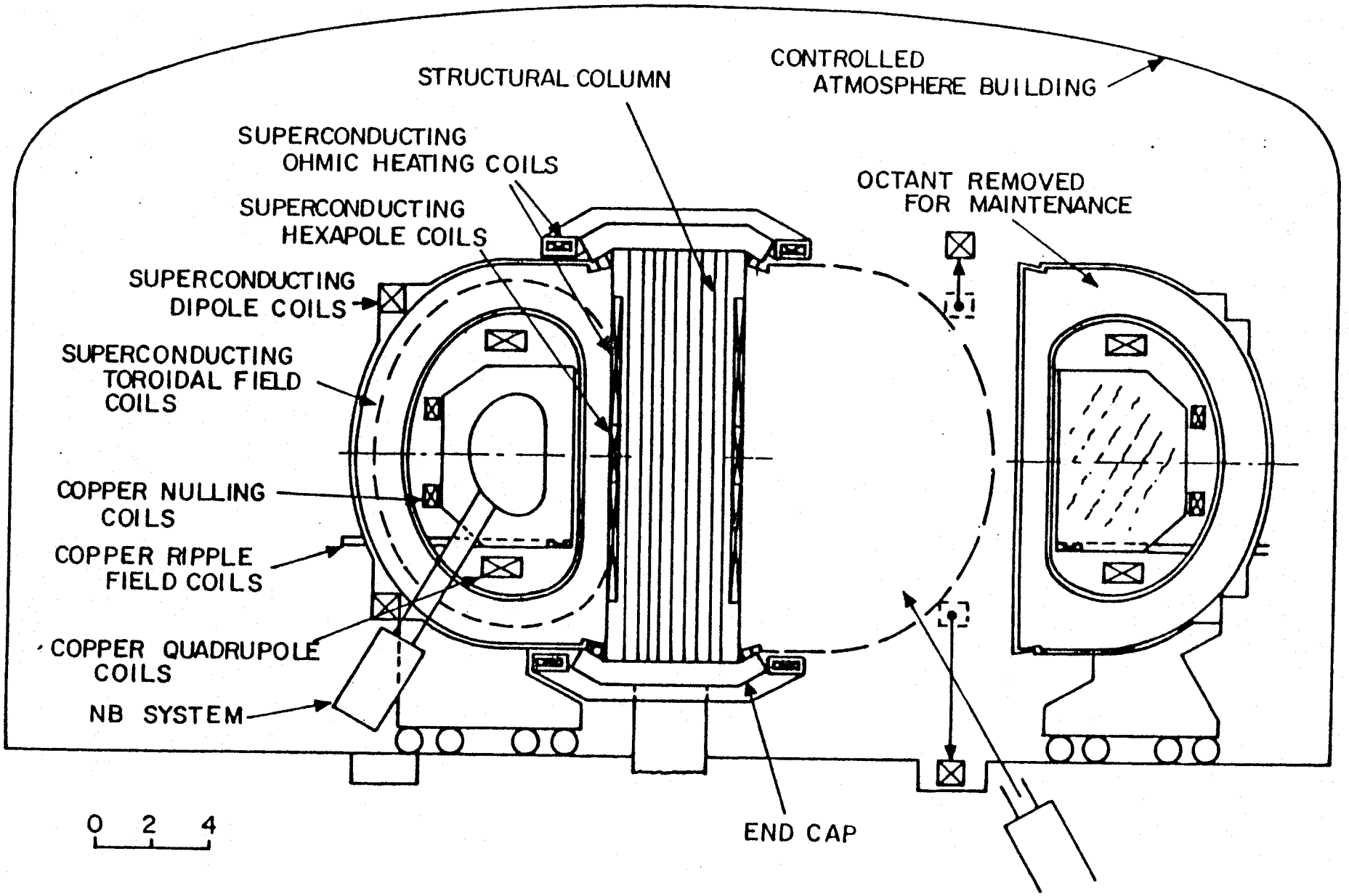

Figure 2 Elevation view of HFCTR showing all magnet systems.

remain cold. This design avoids the necessity of warming the entire magnet system to service one module. The reference helium atmosphere around the entire magnet system eliminates air condensation on the cold surfaces which are accessible through "cracks" between the moveable cryostat walls.

The removal of a module is further simplified by the use of mechanically actuated vacuum seals instead of welds on the vacuum vessel flanges, and by the use of a method of support for out-of-plane forces which does not require the use of shear panels between modules.

The equilibrium field system is chosen to maximize the flexibility of coil location and to reduce the pulsed energy requirement. The main equilibrium field system consists of a superconducting dipole coil outside the toroidal field coils and a DC copper quadrupole coil inside. A nulling field coil, placed inside the toroidal field coils, is driven to oppose the DC vertical field [4]. It is regulated to provide the correct equilibrium field during start-up. The nulling-coil field is decreased as the plasma current increases, simultaneously providing the correct equilibrium field and about half of the required 120 Wb of fast flux. The energy transfer of 500 MJ in this system is only 1/4 that of the total equilibrium field. Figure 1-6 shows the time dependent magnetic flux transfer and the buildup of plasma current.

The copper coils which are located in the TF coil bore, are segmented to permit the withdrawal of a module. Supporting these segments on the blanket and shield structure to eliminate hoop tension makes possible the design of an intersegment connector which can operate at a current density consistent with those to be used in the coils. This connector which is of the zero insertion force type, will accept the position misalignments which are likely to occur between the segment ends and it will have an acceptable life when

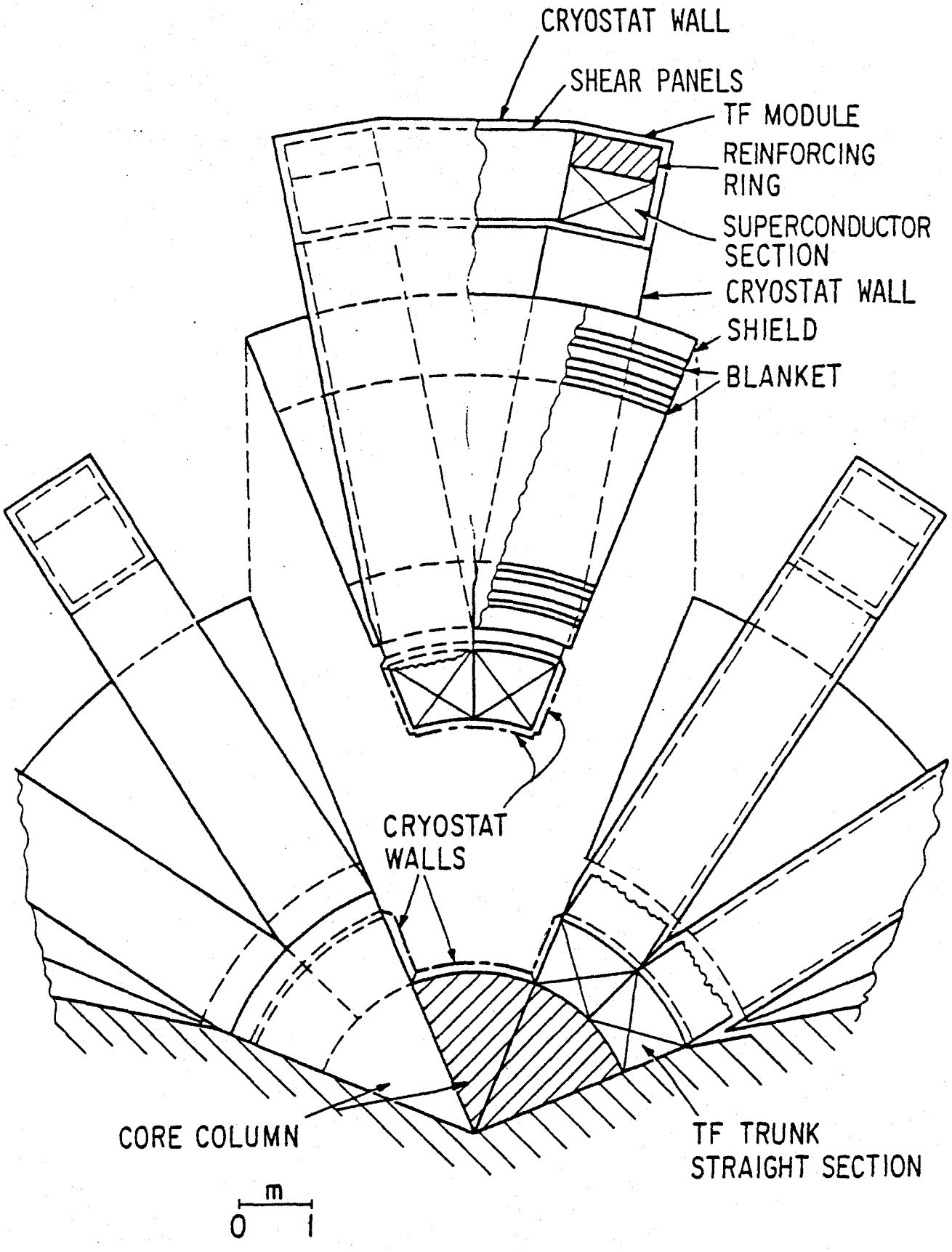

Figure 3 Plan view of toroidal magnet system with a two coil module demounted.

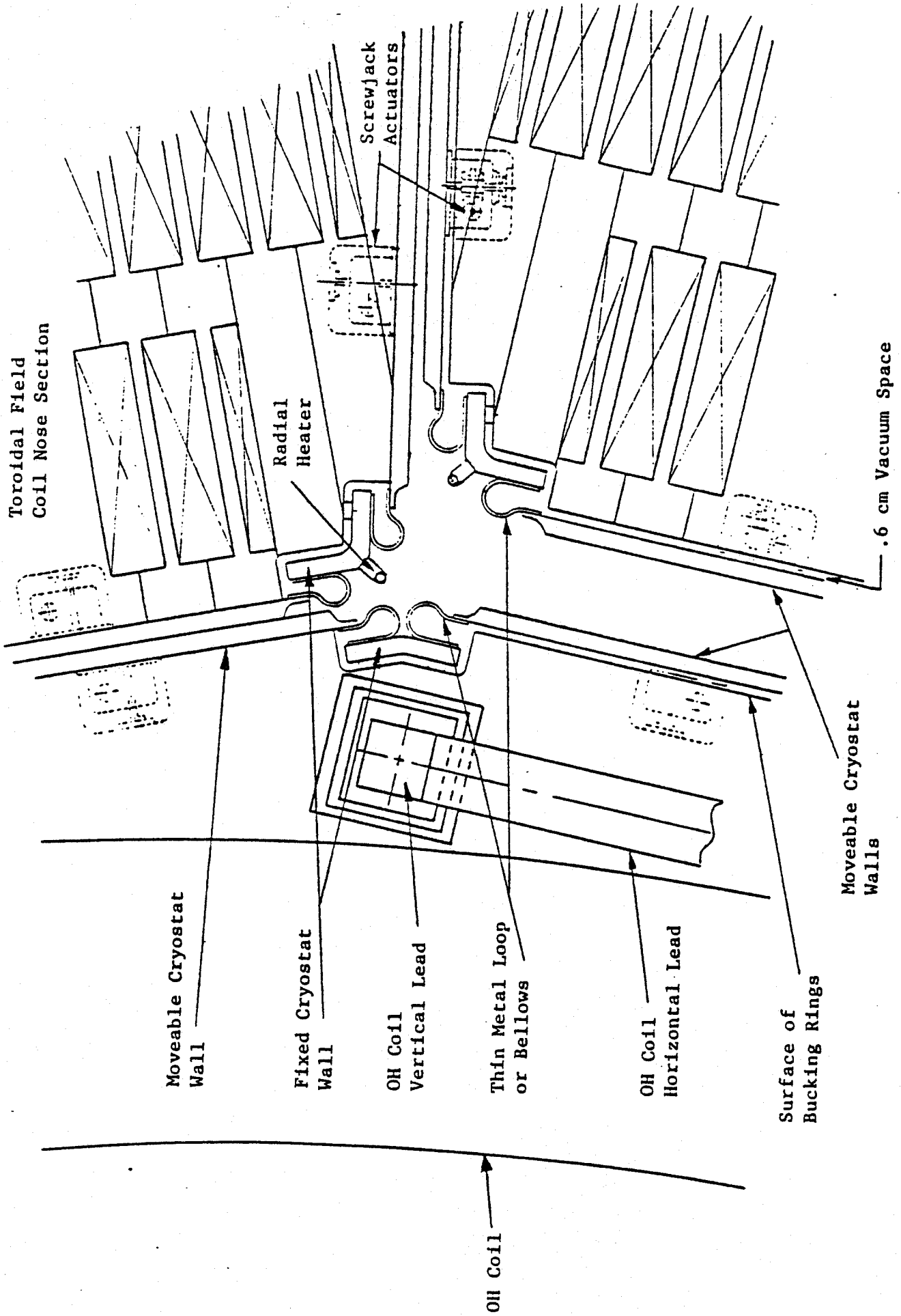

Figure 4 Details of Moveable Cryostat Walls and OH Coil Leads at TF Coil Nose

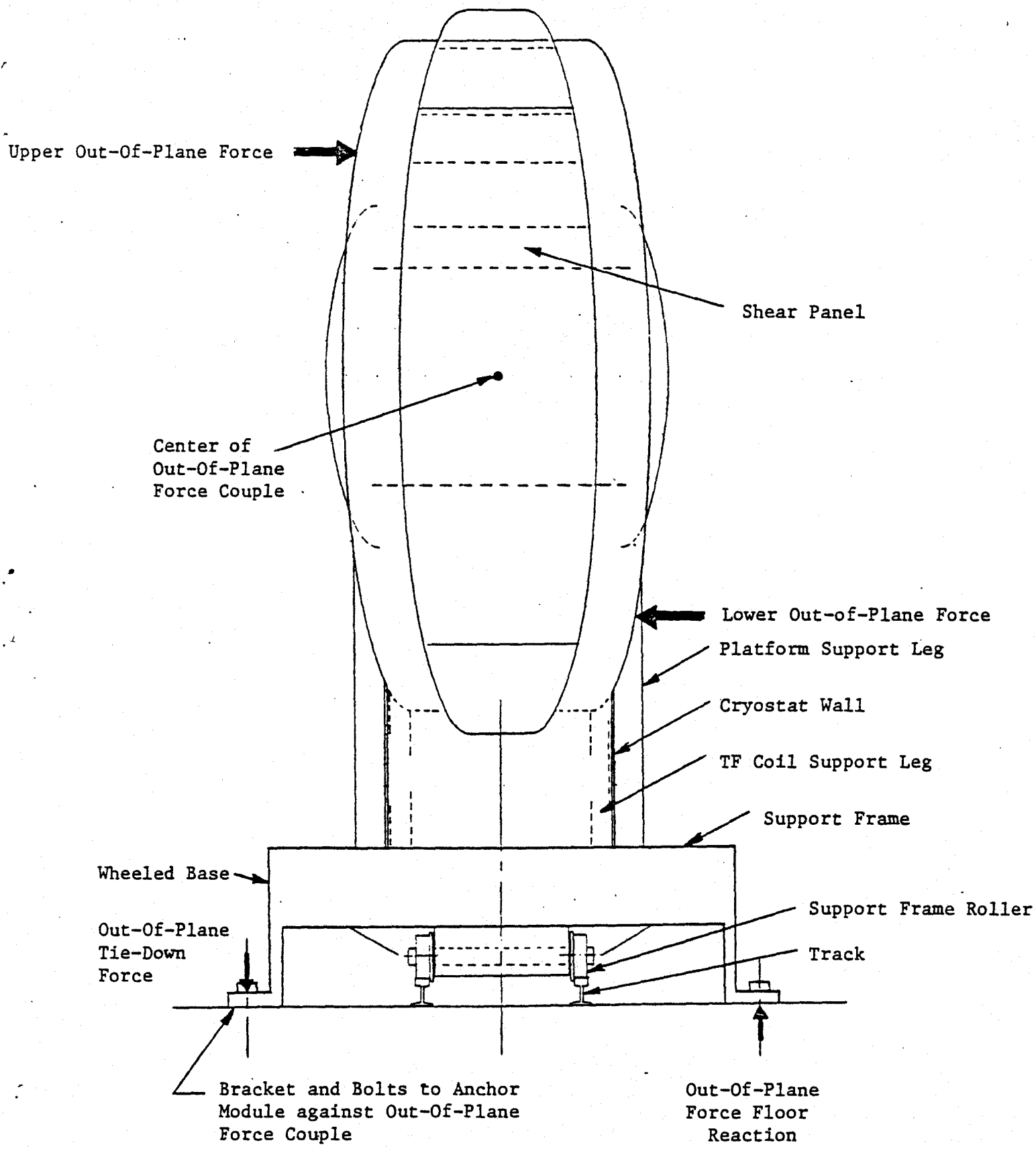

Figure 5-5 View of Module Looking Toward Center of the Toroid

the reactor. This equipment will be in the nature of automatic devices which are built to perform a specific function with minimal human monitoring, instead of manipulators which require a human operator. No manipulators are required for the exchange of a module. However, manipulators in a shielded mobile floor unit are available as a backup in case of a failure of the automatic devices.

5.2 MODULE STRUCTURAL SUPPORT

The details of the construction of a module are shown in Figures 5-3, 5-4, and 5-5. The basic mechanical structure is a wedge shaped box formed by two TF coils and the shear panels which fasten them rigidly together. This box structure is supported on four legs which rest on the wheeled base.

This box construction makes the concept of modularization possible because it provides a way to support the individual TF coils against the out-of-plane forces without having shear panels between the modules. The modules can be removed without having to dismantle shear panels. This greatly simplifies the automation of the module replacement process and greatly simplifies the provision of a cryostat around each individual module. The manner in which the out-of-plane forces on a module are supported is shown in Figure 5-5. The force couple applied to the box by the out-of-plane forces is balanced by clamping the wheeled base solidly to the track which is part

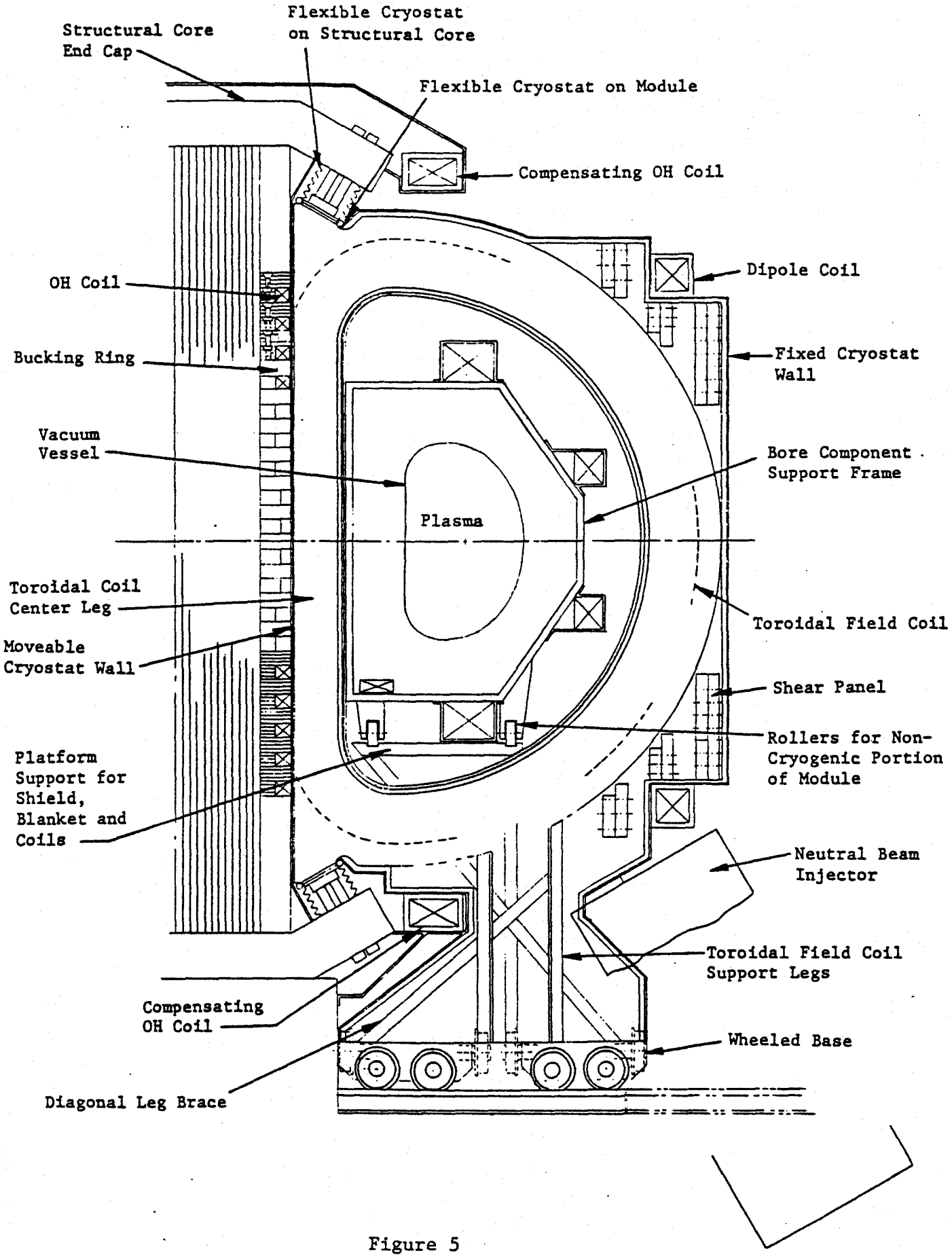

Figure 5

Elevation View of a Module Cross-Section Showing the Module Support System

be required with simple flat surfaces. The spacing between the conductors at the support clamp is such that the contact fingers interleave without any surface pressure between them except for that which is required to spring the flexible copper sheets to obtain vertical alignment. Beveling of the leading edges of the fingers displaces the contact fingers as necessary as the connector halves are engaged. This connector is thus of the "zero insertion force" type which is widely used by the electronic connector industry. Once the fingers are interleaved, the clamp is engaged to squeeze the stack of fingers together and thus properly deflect the many hundreds of contact springs in the Multilam strips. The sheet copper provides the flexibility required as the stack height changes with the application of the clamping pressure. Cooling water is circulated through the conductors and finger plates as shown in Figure 5-10.

This connector design has the advantage that it will tolerate wide misalignment in the horizontal direction. Furthermore it will tolerate the different insertion paths which are obtained depending on which of the two neighboring modules is moved, as illustrated in Figure 5-9. The clamping pressure is insufficient to enable the connector friction to support the hoop tension which develops when the conductors are carrying current. Furthermore, experience with the PDX tokamak at Princeton using fingers without multilams showed that the application of a clamping pressure adequate to take the hoop tension across the joint by friction caused the contact surfaces to weld together so that the connector could not be taken apart. This hoop tension must be supported by automatic clamps which firmly attach the bore component support frame of one module to that of the adjacent module. No matter how firmly these coil segments are supported, there will be some movement of

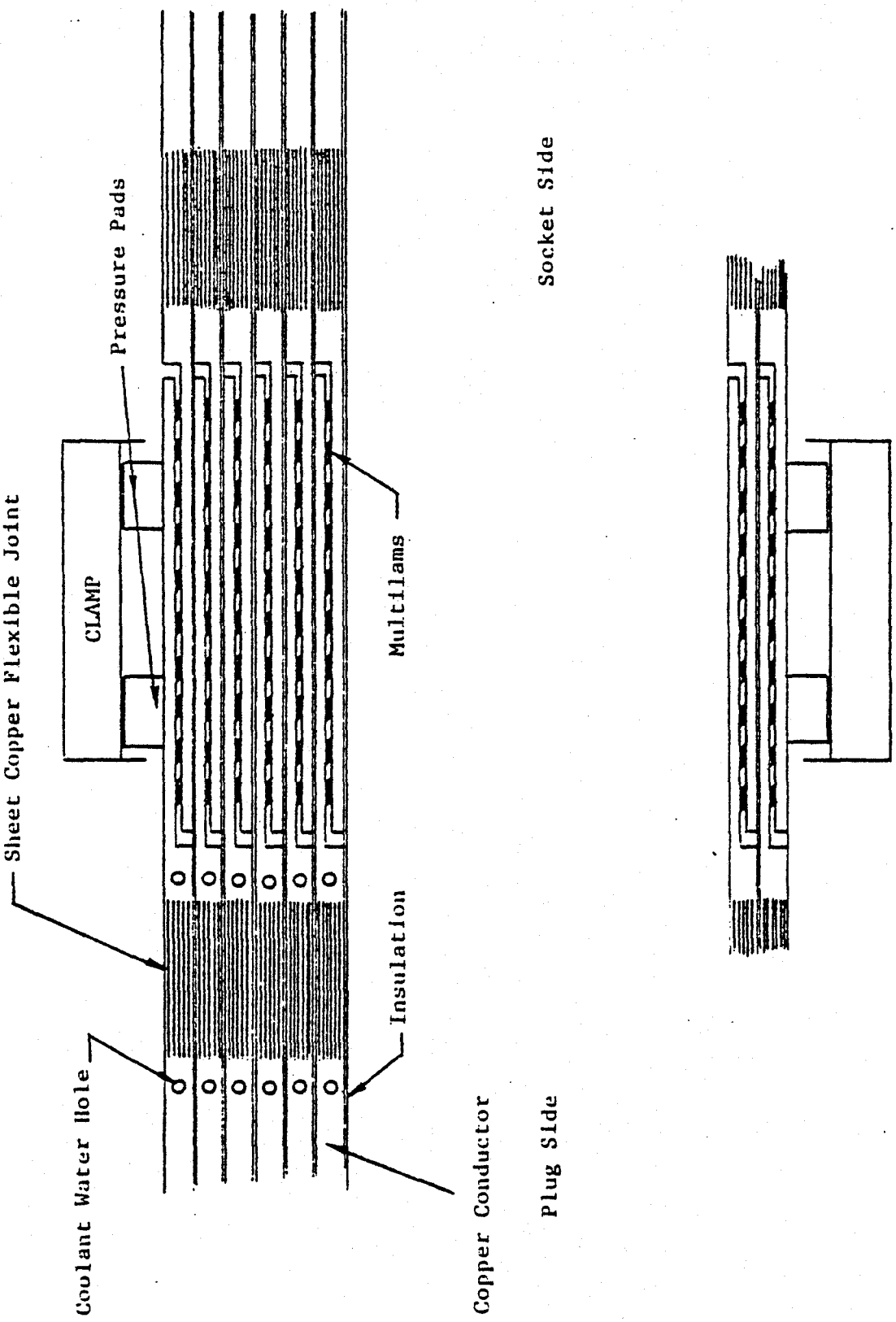

Figure 6 Side View of EF Coil Connector

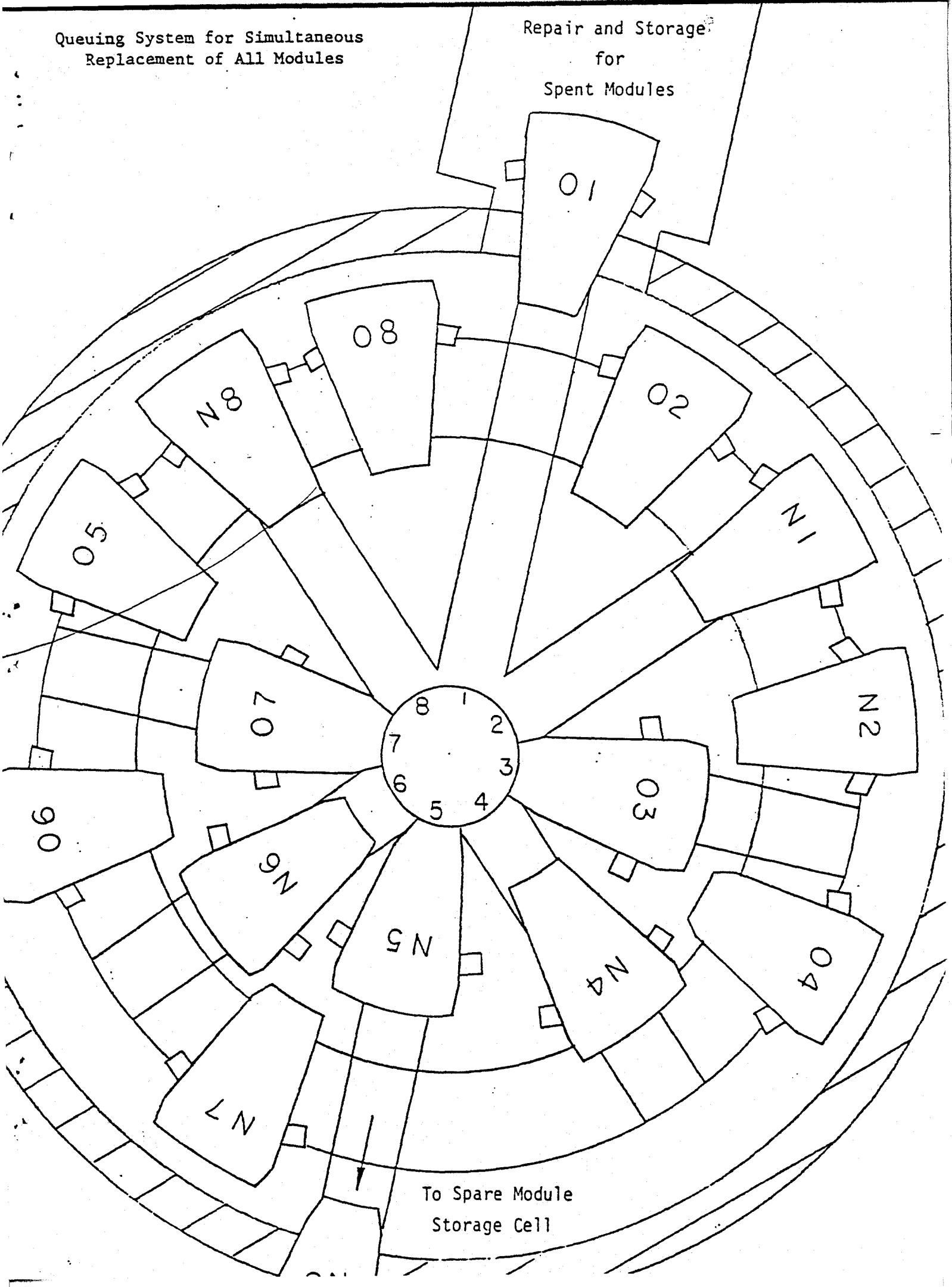
Queuing System for Simultaneous Replacement of All Modules
Repair and Storage for Spent Modules
O1
O2
O3
O4
O5
O6
O7
O8
N1
N2
N4
N5
N6
N7
N8
1
2
3
4
5
6
7
8
To Spare Module Storage Cell

Molybdenum and Chlorine X-Ray Emission from Alcator A

J.E. Rice, E.S. Marmar and T. Coan

Plasma Fusion Center/Francis Bitter National Magnet Laboratory, M.I.T.

S. L. Allen

Johns Hopkins University

R.D. Cowan

Los Alamos Scientific Laboratory

PFC/RR-80-5
PFC/JA-80-1

Abstract

High resolution ($\Delta\lambda/\lambda \simeq .015$) x-ray spectra in the wavelength region 3.7 → 6.2 Å (3.4 → 2.0 keV) have been collected from the Alcator tokamak using a flat crystal Bragg monochromator. Molybdenum L lines and chlorine K lines have been observed and charge state identifications have been made by comparison with calculations.

I. Detection System

A flat crystal monochromator with a pentaerythritol (PET, 2d = 8.742 Å) crystal has been installed on the Alcator A tokamak. A proportional counter was used as the photon detector and overall time resolution of the detection system was about 100 μs. Spectra have been obtained by scanning in wavelength on a shot to shot basis during a sequence of identical discharges. Wavelength calibration was achieved by using the L series of Mo^{II} produced by a Henke tube. Accuracy of wavelength determinations is about $\pm$ .005 Å.

II. Observations on Alcator A

Fig. 1 shows the time history of a typical Alcator A discharge at 60 kG. The top traces are the plasma current and average electron density (50 kA/div and 1 x $10^{14}cm^{-3}$/ fringe). The third trace is the monochromator signal at 4.76 Å (2.60 keV) and the bottom trace is the total soft x-ray flux above 1.5 keV from a surface barrier diode (SBD) viewing along a chord through the center of the plasma. The time scale is 20 ms/div. During the steady state portion of this discharge, when the average electron density was 2.9 x $10^{14}cm^{-3}$, the plasma current was 160 kA, and the sawtooth oscillations were well developed (between 70 and 110 ms), the central electron temperature was $\sim$ 900 eV. At the startup phase of the discharge, around 20 ms when the

density was 5 x 10^{13} cm^{-3}, the electron distribution was non-thermal but (in the energy region of interest) can be characterized by a hot Maxwellian with $T_e \sim 1800$ eV. Note the large spike on the SBD and spectrometer signals at this time.

Fig. 2 is the spectrum at 100 ms for a series of discharges similar to the one shown in Fig. 1, obtained by scanning in wavelength on a shot to shot basis. Shown for comparison are the gf values for the strongest 2p-3d transitions in Mo^{23+} and Mo^{24+}. These gf values were computed using the HXR method of calculating radial wavefunctions, including the Slater-Condon theory of atomic structure[1,2]. The bumps at 4.9 and 5.1 Å are in good agreement with the predicted 2p-3d lines of Mo^{23+} and Mo^{24+}, supportive of coronal equilibrium calculations[3] which predict the predominant molybdenum charge states at 900 eV to be near Mo^{23+} and Mo^{24+}.

Fig. 3 is the spectrum at 20 ms, during the spike of the SBD signal. Shown for comparison are the predicted gf values for the 2s-3p, 2p-3d, and 2p-3s transitions of Mo^{32+} and Mo^{31+} as well as the 2p-3d transitions for Mo^{30+}. Again, the wavelength agreement is quite good. The relative heights of the observed 2p-3s lines to the 2p-3d lines are considerably larger than the gf value ratio. This has been observed elsewhere[4] for Mo^{32+}. These charge state identifications are again in agreement with coronal equilibrium calculations[3] which predict the predominant charge states at 1800 eV to be Mo^{30+}, Mo^{31+}, and Mo^{32+}. However, this

is neither a steady state nor thermal portion of the discharge and these particular coronal equilibrium calculations are not necessarily a priori valid.

There remains to explain the feature at 4.44 Å (2.79 keV) in Fig. 2. Fig. 4 exhibits a more detailed scan of this feature for discharges similar to the one described above. Also shown are the predicted wavelengths for the K lines of heliumlike Cl^{15+}[5]. The agreement is quite good. Again, coronal equilibrium calculations[3] suggest that the predominant charge state for 400 eV $\leq T_e \leq$ 1500 eV is Cl^{15+}. This is consistent with the observation on Alcator A that this line prevails for a range of central electron temperature between 700 and 1200 eV. The molybdenum features between 4.6 and 5.1 Å shift as the electron temperature is altered as expected from changes in charge states. These observations support both the wavelength predictions and the coronal equilibrium calculations.

Chlorine radiation has been seen in the UV and visible regions as well. In particular, the 2s-2p transition of Cl^{14+} at 384 Å and the 3s-3p transitions of Cl^{6+} at 813 and 801 Å have been observed with a spatial imaging detection system (SIDS)[6]. Fig. 5 is a spatial brightness profile of the 384 Å line. The points outside $\pm$ 5 cm represent contamination from the bright C^{IV} line also at 384 Å but located at a larger radial position. The 4795 Å line of Cl^{II} has been observed during discharge cleaning. The 384 Å line has been seen in TFR[7] discharges.

A possible source for the chlorine is the solvent trichloroethane used in cleaning Alcator vacuum components. Chlorine may also be a contaminant of the stainless steel vacuum bellows. The source of the molybdenum is the Mo limiter used in Alcator A. Further evidence that the 4.44 Å feature is not due to molybdenum radiation has been provided by a series of impurity injection experiments. In one such case Mo was introduced into the plasma by the laser blowoff technique[8], and Fig. 6a demonstrates the result. The top trace is the average electron density and the rise of the spike in the second trace indicates the time of the laser firing which injected the molybdenum. The third trace is the SBD flux ($h\nu > 1.5$ keV) which exhibits a bump similar to that shown in Fig. 1. The fourth trace is the spectrometer signal at 5.20 Å (2.38 keV) showing a factor of 8 or so increase in signal after the injection. Fig. 6b is a blowup of Fig. 6a near the region of interest (2 ms/div). It seems to take about 6 - 10 ms for the molybdenum to reach the center of the discharge after the injection and the molybdenum remains in the plasma for about 15 ms. Fig. 7 shows a similar trace but with the spectrometer set on 4.44 Å. The SBD trace demonstrates the induced Mo radiation at $\sim$ 50 ms as well as the naturally occuring bump at 25 ms. Neither of these features is present on the 4.44 Å trace indicating that this line is not due to molybdenum.

On the bottom of Fig. 2, an X indicates an observed increase in signal at that wavelength when molybdenum is injected into the plasma and an 0 indicates no change.

From the strength of the Cl K line above the continuum background, one may deduce an estimate of the chlorine density in Alcator A. If one equates the ratio of the observed line to continuum to the ratio of the number of 1s vacancies in[9] Cl^{15+} to the number of continuum photons[10] produced, one obtains (ignoring profile effects)

$$\frac{I_{Cl}}{I_{cont}} = \frac{\dfrac{1.6 \times 10^{-5}\, n_e\, n_{Cl}\, \langle g \rangle\, f_{nn^*}\, e^{-\Delta E/T_e}}{\Delta E \sqrt{T_e}}}{\dfrac{9.58 \times 10^{-14}\, n_e^{\,2}\, \xi \bar{g}\, e^{-h\nu/T_e}\, \Delta h\nu}{h\nu \sqrt{T_e}}} \qquad (1)$$

where f_{nn^*} is the oscillator strength of the transition of energy ΔE, $\langle g \rangle$ and $\bar{g}$ are gaunt factors, ξ is the bremsstrahlung enhancement factor, and $\Delta h\nu$ is the resolution of the instrument. Solving for n_{Cl} and taking $I_{Cl}/I_{cont} = 9$, $n_e = 3 \times 10^{14} cm^{-3}$, $\xi = 1$, $\langle g \rangle = .2$, $f_{nn^*} = .8$, $\bar{g} = .7$, $T_e = 900$ eV, $\Delta h\nu = 40$ eV, and $\Delta E = h\nu = 2.79$ keV, one obtains a chlorine density of $3 \times 10^{9} cm^{-3}$ or $10^{-5} n_e$.

From this amount of chlorine, an estimate may be made of its contribution to radiative power loss in the plasma. Taking the cooling rate of chlorine at 900 eV to be 2.5×10^{-27} watt/cm^3 (this is actually the value for sulphur[11]), and electron and chlorine densities to be $3 \times 10^{14} cm^{-3}$ and $3 \times 10^{9} cm^{-3}$, respectively, one obtains a radiated power density of .0023 watt/cm^3 from the center of the plasma. This is a mere .015% of the central input ohmic power density for the

typical case of 15 watt/cm^3, and chlorine does not enter in a significant way to power balance in Alcator A.

III. Conclusions

Observations of Mo L lines from $Mo^{22+} \leq Mo^{i+} \leq Mo^{32+}$ and Cl K lines from Cl^{15+} have been made on the Alcator A tokamak, supportive both of wavelength predictions and coronal equilibrium calculations. Estimates indicate that n_{Cl}/n_e is of order 10^{-5}, therefore not important in power balance considerations.

IV. Acknowledgements

Thanks are due Herb Schnopper for providing the instrument used in these measurements, Dave Stallard for technical support, and Dave Overskei for operating Alcator A.

References

1. R.D. Cowan and D.C. Griffin, J. Opt. Soc. Am. 66, 1010 (1976).

2. R.D. Cowan, J. Opt. Soc. Am. 58, 808, 924 (1968).

3. C. Breton, C. DeMichelis, M. Finkenthal, and M. Mattioli, EUR - CEA - FC - 948 (1978).

4. P. Burkhalter, R. Schneider, C.M. Dozier and R.D. Cowan, Phys. Rev. A 18, 718 (1978).

5. R.L. Kelly and L.J. Palumbo, NRL Report 7599 (1973).

6. R.K. Richards, H.W. Moos, and S.L. Allen, Rev. Sci. Instr. 51, 1 (1980).

7. Equipe TFR CUR - CEA - FC - 984 (1979).

8. E.S. Marmar, J.L. Cecchi and S.A. Cohen, Rev. Sci. Intr. 46, 1149 (1975).

9. R.C. Elton, Methods of Experimental Physics, Vol. 9, Part A, p. 115, Academic Press, 1970.

10. J. Greene, Ap. J. 130, 693 (1959)

11. D.E. Post, R.V. Jensen, C.B. Tartar, W.H. Grasberger and W.A. Locke, Atomic Data and Nucl. Tables 20, No. 5, 397 (1977).

Figure Captions

Fig. 1. Typical 60 kG Alcator A discharge. Top trace 50 kA/div, second trace 1 x $10^{14}cm^{-3}$/fringe, time scale 20 ms/div.

Fig. 2. Brightness vs. wavelength at 100 ms for discharges similar to Fig. 1. Predicted gf values for 2p-3d transitions in Mo^{23+} and Mo^{24+}.

Fig. 3. Spectrum at 20 ms. Predicted gf values for Mo^{30+}, Mo^{31+}, and Mo^{32+} L lines.

Fig. 4. More detailed scan of Cl^{15+} K lines near 4.44 Å.

Fig. 5. Radial brightness profile at 384 Å.

Fig. 6a. Molybdenum injection, 20 ms/div. 6b. Expanded view of injection, 2 ms/div.

Fig. 7. Molybdenum injection showing no effect at 4.44 Å.

Typical Alcator A Discharge at 60 KG

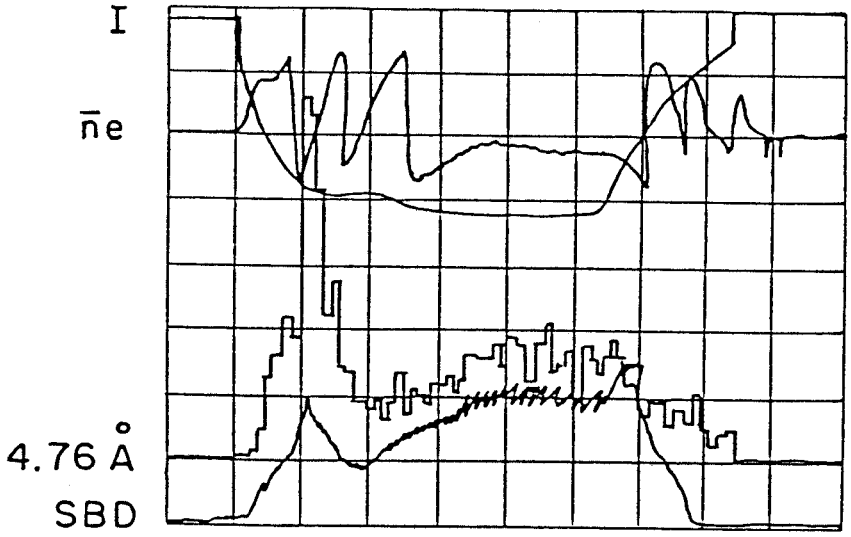

Fig. 1.

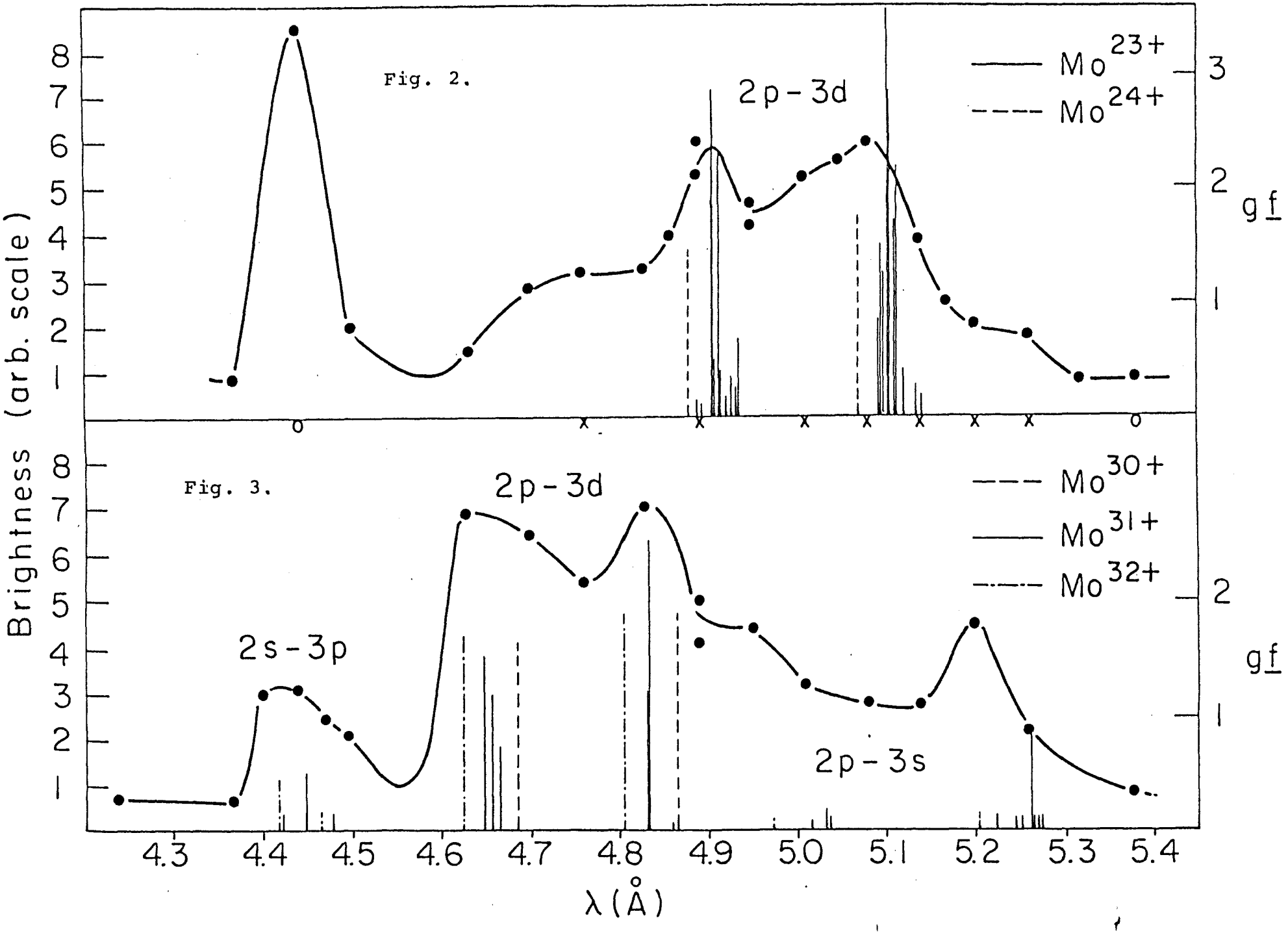
Fig. 2.
2p - 3d
Mo 23+
Mo 24+
Fig. 3.
2p - 3d
Mo 30+
Mo 31+
Mo 32+
2s - 3p
2p - 3s
Brightness (arb. scale)
gf
λ (Å)
4.3
4.4
4.5
4.6
4.7
4.8
4.9
5.0
5.1
5.2
5.3
5.4

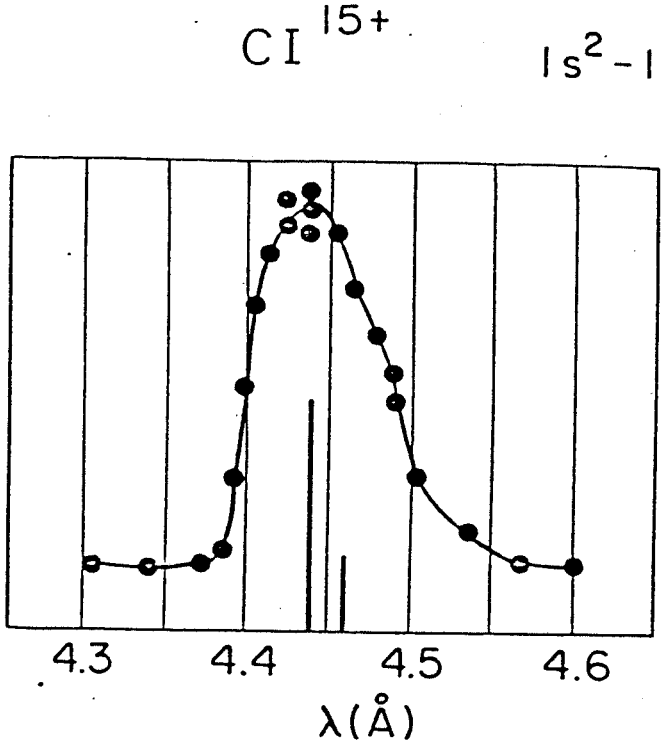

Fig. 4.

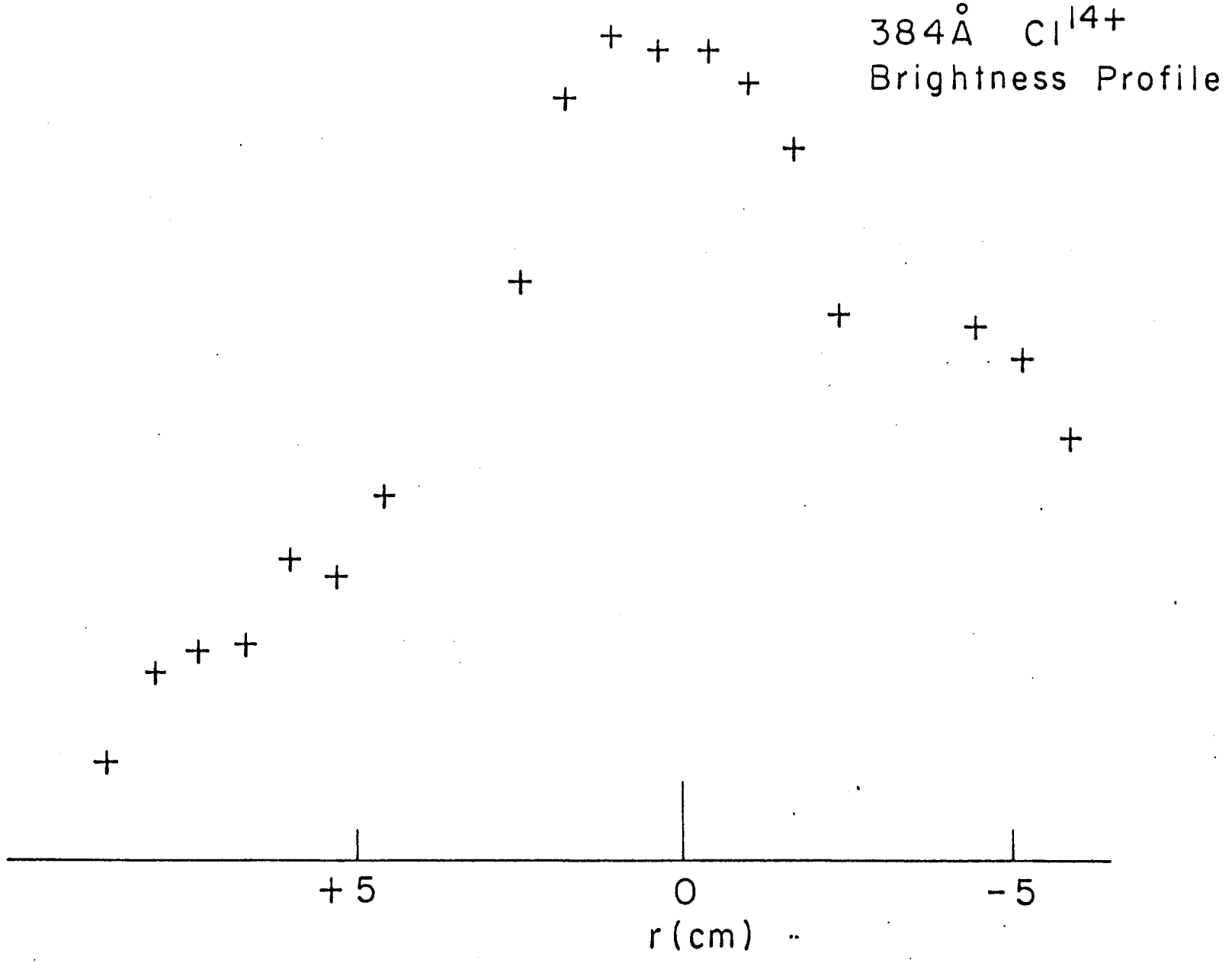

Fig. 5.

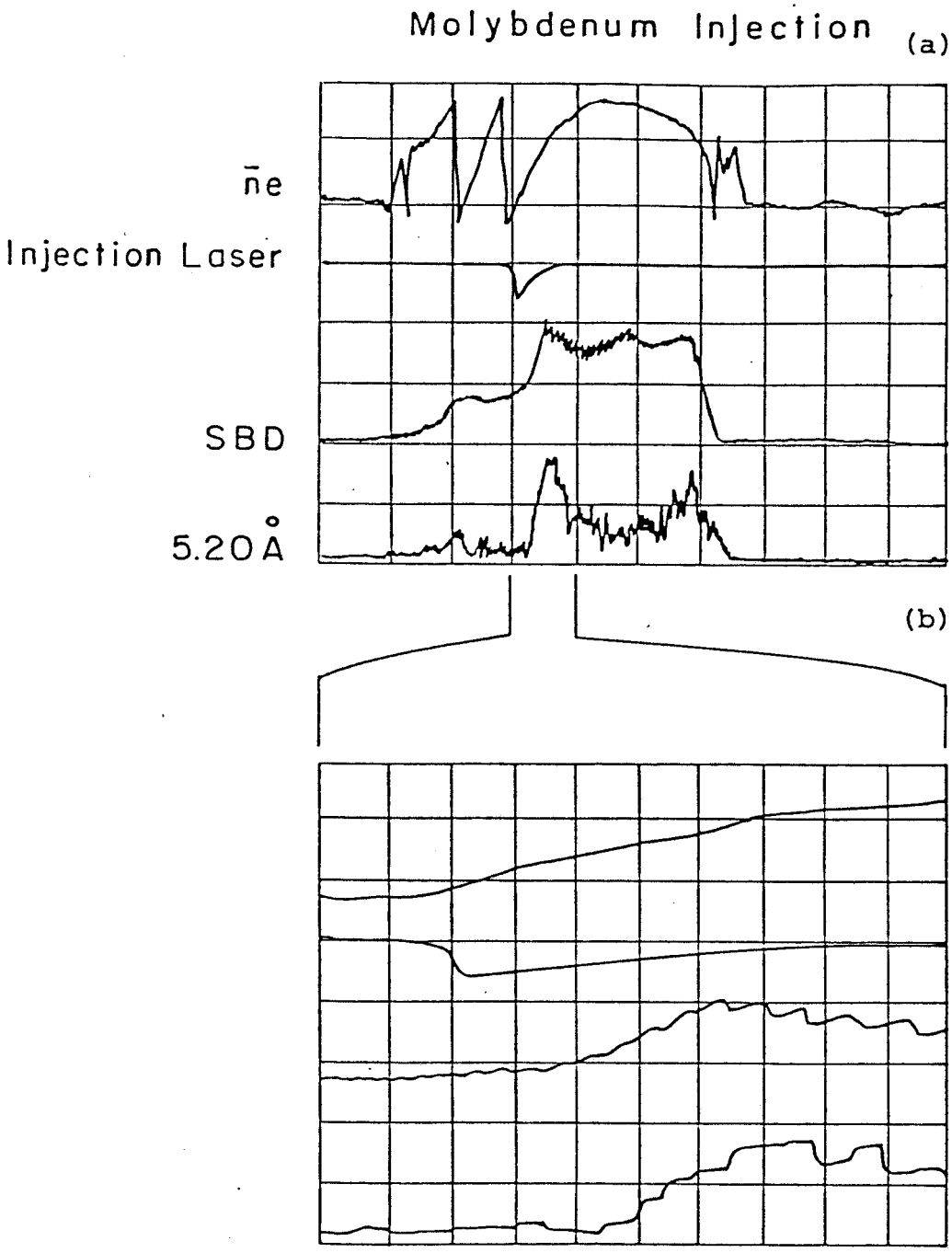

Fig. 6.

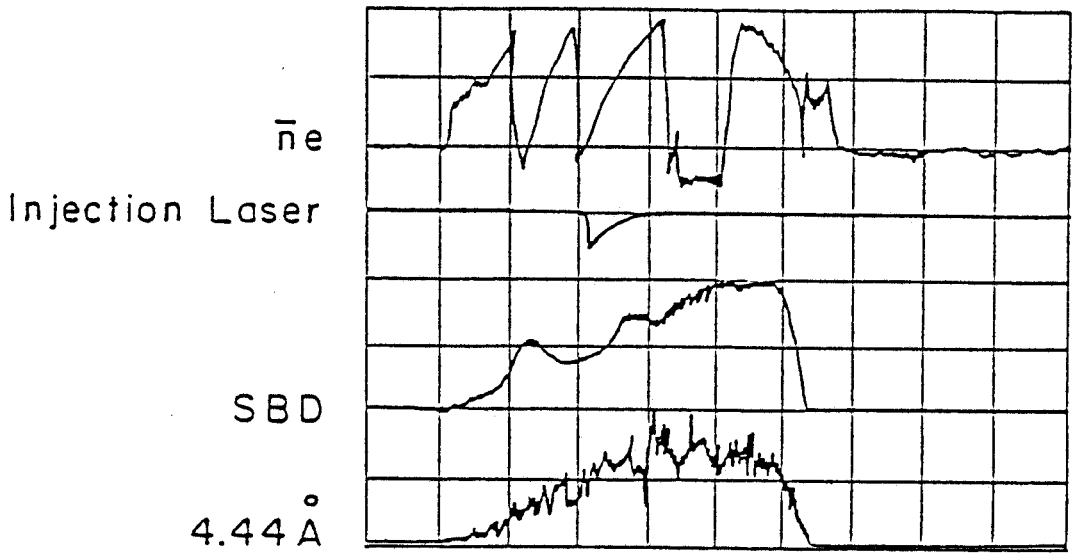

Fig. 7.